



# High-energy asymmetric supercapacitor based on petal-shaped MnO<sub>2</sub> nanosheet and carbon nanotube-embedded polyacrylonitrile-based carbon nanofiber working at 2 V in aqueous neutral electrolyte

Chen-Hao Wang\*, Hsin-Cheng Hsu, Jin-Hao Hu

*Department of Materials Science and Engineering, National Taiwan University of Science and Technology, Taipei 10607, Taiwan*



## HIGHLIGHTS

- The ASC uses petal-shaped MnO<sub>2</sub> and a network of CNT-CNF as the electrodes.
- The ASC shows a high specific capacitance in an aqueous neutral electrolyte.
- The ASC shows a high power density by operating at a cell voltage of 2.0 V.
- The ASC is attributed to the synergistic effects of the two superior electrodes.

## ARTICLE INFO

### Article history:

Received 23 August 2013

Received in revised form

17 September 2013

Accepted 17 October 2013

Available online 25 October 2013

### Keywords:

Nanoparticles

Nanostructures

Electrochemistry

Asymmetric supercapacitors

Manganese dioxides

## ABSTRACT

An asymmetric supercapacitor (ASC) uses very thin petal-shaped MnO<sub>2</sub> nanosheets as the positive electrode and a network of carbon nanotube-embedded polyacrylonitrile-based carbon nanofibers (CNT-CNF electrodes) as the negative electrode. It has a high specific capacitance and a high specific energy density in 0.5 M Na<sub>2</sub>SO<sub>4</sub>. An assembled MnO<sub>2</sub>/CNT-CNF ASC is operated reversibly at a high cell voltage of 2.0 V and exhibits a high specific capacitance of 93.99 F g<sup>-1</sup> and an excellent energy density of 52.22 Wh kg<sup>-1</sup>, which is better than those of ASCs that are based on MnO<sub>2</sub>/carbon, which can be found in the literature. The MnO<sub>2</sub>/CNT-CNF ASC has superior cycling stability with 92% retention of initial specific capacitance after 2000 cycles.

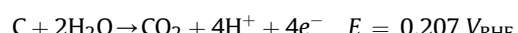
© 2013 Elsevier B.V. All rights reserved.

## 1. Introduction

Supercapacitors or electrochemical capacitors are promising energy storage devices because of their high power density, fast charging and discharging, and long cycle life. They have attracted much attention for a wide range of applications from electrical or hybrid vehicles, renewable energy generation devices, and portable devices. However, the energy density of a commercially symmetric supercapacitor is typically less than 10 Wh kg<sup>-1</sup>, which is lower than that of a battery [1–3]. The following equation gives the energy density (*E*) of a supercapacitor,

$$E = \frac{1}{2}CV^2 \quad (1)$$

where *E*, *C* and *V* are the energy density, the specific capacitance and the cell voltage, respectively. The energy density of a supercapacitor can be improved by increasing the cell potential. Some investigations have utilized organic electrolytes, which have wide voltage windows, in cells [4–6]. However, most organic electrolytes have poor ionic conductivity and high cost; raise environmental concerns, and can be used only in cells that are fabricated in an oxygen-free environment. Some works have developed high-voltage symmetric supercapacitors in aqueous electrolytes [7–9]. However, high-voltage operation may corrode carbon-based materials, especially in positive electrodes, as follows.



An asymmetric supercapacitor (ASC) comprises a

\* Corresponding author. Tel.: +886 2 2730 3715; fax: +886 2 2737 6544.

E-mail address: [chwang@mail.ntust.edu.tw](mailto:chwang@mail.ntust.edu.tw) (C.-H. Wang).

pseudocapacitive electrode and an electrochemical double-layer electrode, which has the advantages of both supercapacitor (rate and cycle life) and battery (energy) [10]. When the positive and negative electrodes are carefully operated with different potential windows, the ASC can be operated with a cell voltage of up to 2.0 V in aqueous electrolyte.

The positive materials in ASCs can be metal oxides (such as RuO<sub>2</sub> and MnO<sub>2</sub>) and conducting polymers (such as polyaniline and PEDOT), whose electrochemical behaviors are pseudocapacitive [11]. Given its cost and environmental friendliness, MnO<sub>2</sub> is a feasible material for use as a positive electrode in a supercapacitor [12]. MnO<sub>2</sub> is an abundant non-toxic raw material with a low cost, and has been utilized in a primary alkaline battery (Zn/MnO<sub>2</sub>) as an active cathode material. The thermodynamically reversible voltage of water evolution is 1.23 V. The overpotentials of oxygen and hydrogen evolutions in the aqueous electrolyte depend strongly on pH. Khomenko et al. plotted a potential-pH graph for the evolution of O<sub>2</sub> on α-MnO<sub>2</sub> and that of H<sub>2</sub> on activated carbon, and found that the cell voltage window may extend to 2 V at pH values of 6–7 [13]. MnO<sub>2</sub> has several crystallographic forms, which are known as α, β, γ, δ, and λ. The structures of α, β, and γ include 1D tunnels; the δ form has a 2D layered structure and the λ form has a 3D spinel structure. Since the specific capacitance depends on the degree of intercalation/deintercalation of protons or cations into/from the MnO<sub>2</sub> lattice, the different crystallographic forms are expected to have different capacitive properties. Brousse et al. studied various crystallographic forms of MnO<sub>2</sub> and their specific capacitances in 0.1 M K<sub>2</sub>SO<sub>4</sub> [14]. They found values for the β, γ, δ and λ structures of 5, 30, 80–110, and 70 F g<sup>-1</sup>, respectively; the δ-MnO<sub>2</sub> had the better specific capacitance. Devaraj and Munichandraiah studied the specific capacitances of α, β, γ, and δ structures in 0.1 M Na<sub>2</sub>SO<sub>4</sub>, and found that the α-MnO<sub>2</sub> (241–297 F g<sup>-1</sup>) had the best [15].

The negative materials of ASCs are carbon-based. They include activated carbon, carbon nanotubes (CNT), and graphene, which store energy by charge separation at the interface between the electrolyte and the electrode, which is called the electrochemical double-layer mechanism [1,16–24]. The specific capacitance of a carbon-based material is generally assumed to be like that of a parallel-plate capacitor:

$$C = \frac{\epsilon_r \epsilon_0}{d} A \quad (2)$$

where  $\epsilon_r$ ,  $\epsilon_0$ ,  $A$  and  $d$  are the electrolyte dielectric constant, the permittivity of a vacuum, the specific surface area of the electrode that is accessible to the electrolyte ions, and the Debye length. Accordingly, the specific capacitance of the carbon-based material depends on its specific surface area and electrical conductivity, as well as the type of electrolyte with which it is used [25]. Zhang et al. reviewed various carbon-based materials, and found that the typical specific capacitances of activated carbon, CNTs, and graphene were approximately <200, 50–100, and 100–150 F g<sup>-1</sup>, respectively, in aqueous solution [26,27]. Wang et al. studied curved graphene nanosheets (CGN) in various aqueous media, and found that the specific capacitances of CGNs were about 120, 150, and 75 F g<sup>-1</sup> in 6 M KOH, 1 M H<sub>2</sub>SO<sub>4</sub>, and 1 M Na<sub>2</sub>SO<sub>4</sub>, respectively [28]. The specific capacitance of carbon-based material in neutral solution (Na<sub>2</sub>SO<sub>4</sub>) was half of that in an acidic medium (H<sub>2</sub>SO<sub>4</sub>) and 62.5% of that in a basic medium (KOH). Several studies have found similar results [8,29].

Carbon nanofibers (CNFs) with high surface areas and porosities have attracted much attention in recent years and are considered to be promising candidates for energy applications [30]. CNFs can be produced by several techniques, of which electrospinning is particularly low-cost and versatile [31]. Guo et al. studied hybrid

CNFs that contained CNTs that were produced by electrospinning; they had a specific capacitance of 310 F g<sup>-1</sup> in 1.0 M H<sub>2</sub>SO<sub>4</sub> [32]. Zhou et al. used electrospun CNFs surface-grafted with vapor-grown CNTs as hierarchical electrodes for supercapacitors, and found a specific capacitance of 185 F g<sup>-1</sup> in PVA/H<sub>3</sub>PO<sub>4</sub> gel electrolyte [33]. Hsu et al. demonstrated the directly grown graphene-like carbon nanowall (GNW)–CNT–polyacrylonitrile-based CNF paper structure, and obtained a specific capacitance of 176 F g<sup>-1</sup> in 0.5 M H<sub>2</sub>SO<sub>4</sub> [34]. They stated that CNTs and graphenes had excellent electrical conductivity, and thus hybrid carbon composites that contained CNTs and graphenes provided improved electrical conductive pathways for charge transfer in the electrodes, significantly increasing specific capacitance. These reports only measured CNF-based materials by using three-electrode cells or symmetric capacitor setups in acid or alkaline media. However, CNF-based materials that were used in ASCs and neutral medium were rarely reported in the literature.

This work reports on an MnO<sub>2</sub>//CNT-CNF ASC in which the MnO<sub>2</sub> nanocomposite is used as the positive material and the CNT-embedded polyacrylonitrile-based CNF (CNT-CNF electrode) is used as the negative electrode. The as-prepared ASC can be reversibly charged and discharged at 2.0 V in 0.5 M Na<sub>2</sub>SO<sub>4</sub>, exhibiting a high specific capacitance of 93.99 F g<sup>-1</sup> with an excellent energy density of 52.22 Wh kg<sup>-1</sup> at a current density of 0.1 A g<sup>-1</sup>. The as-prepared ASC also has a superior cycling stability with the retention of approximately 92% after 2000 cycles.

## 2. Experimental

### 2.1. Preparation of α-MnO<sub>2</sub> and δ-MnO<sub>2</sub>

The preparations of α-MnO<sub>2</sub> and δ-MnO<sub>2</sub> were modified from those of Yang and Huang [35]. All chemicals used in this experiment were analytical grade. To prepare α-MnO<sub>2</sub>, MnSO<sub>4</sub> (0.01 mol) and KMnO<sub>4</sub> (0.01 mol) were mixed in deionized water (100 mL) and stirred with a magnetic stirrer for 10 min to yield a homogenous solution at room temperature. Then, the solution was transferred to a Teflon-lined stainless steel autoclave with a 120 mL capacity, which was loaded into an oven that had been preheated to 140 °C for 2 h. Thereafter, the pressure vessel was cooled by natural convection. The precipitates were filtered and washed in deionized water and ethanol to remove unreacted materials. The precipitates were dried overnight at 60 °C in air. To prepare δ-MnO<sub>2</sub>, MnSO<sub>4</sub> (0.01 mol) and KMnO<sub>4</sub> (0.03 mol) were mixed in 100 mL deionized water, and the above steps were followed.

The positive electrode was prepared by mixing active materials (70 wt%, α-MnO<sub>2</sub> and δ-MnO<sub>2</sub>), activated carbon (20 wt%) and polyvinylidene fluoride (10 wt%) in N-methyl-2-pyrrolidone, and then the slurry was treated by a homogenizer. The homogenized slurry was spread onto nickel foil with a loading of 1.0 mg cm<sup>-2</sup>. The electrode was heated at 110 °C for 12 h to eliminate the solvent.

### 2.2. Preparation of CNT-embedded polyacrylonitrile-based carbon nanofiber

Polyacrylonitrile-based CNF (CNF electrode) and CNT-embedded polyacrylonitrile-based CNF (CNT-CNF electrode) were prepared by electrospinning in an electric field that was established by applying a 20 kV electrical potential across a 22 cm gap between a syringe and a collector. To prepare the CNF electrode, the spraying solution was polyacrylonitrile (50 wt%) in DMF. To prepare the CNT-CNF electrode, the spraying solution was 3 wt% commercial CNT and polyacrylonitrile (50 wt%) in DMF. Following the electrospinning process, the sample was treated in a tubular furnace for the oxidative stabilization at 280 °C in air for 2 h. It was then heated

to 800 °C at a rate of 1 °C min<sup>-1</sup> for 30 min in an atmosphere of argon to complete the carbonization.

### 2.3. Analysis of materials

X-ray diffraction measurements were made on a Bruker D8 advanced high-resolution diffractometer system with Cu K $\alpha$  radiation at 1.54056 Å, scanning from 10°–80° (2 $\theta$ ) at a scan rate of 1° min<sup>-1</sup> in steps of 0.02° at room temperature. The morphology of the sample was observed using a high-resolution scanning electron microscope (HRSEM, JEOL-6700F). A field-emission TEM/STEM (JEOL-2100) with an energy-dispersive detector (EDS) was used to observe the micro-structure of the sample. Nitrogen adsorption–desorption isotherms were obtained using a Tristar 3000. Before the measurements were made, the samples were degassed at 100 °C in a vacuum for 5 h. Brumauer–Emmett–Teller (BET) measurements were made to estimate the specific surface area ( $S_{BET}$ ). The resistance of the samples was measured in a two-electrode holder by performing an AC impedance analysis.

### 2.4. Electrochemical measurement

The sample was placed in a holder as a working electrode, which was connected to the electrochemical instrument (Solartron 1280C) via a golden wire. In making the three-electrode measurements, the reference electrode was an SCE electrode (0.242 V vs. SHE) and the counter electrode was a platinum foil. The electrolyte was nitrogen-purged 0.5 M Na<sub>2</sub>SO<sub>4</sub>. In making the two-electrode measurements, the ASC was assembled in a sandwich-type two-electrode coin cell (CR2032 size) using an MnO<sub>2</sub> electrode and a CNT-CNF electrode as the positive and negative electrodes, respectively, which was separated by a separator. The electrolyte was 0.5 M Na<sub>2</sub>SO<sub>4</sub>. The mass of each sample was measured before the electrochemical measurements were made.

## 3. Results and discussion

MnO<sub>2</sub> is composed of basic MnO<sub>6</sub> octahedral units. The sharing of different vertices and edges among the MnO<sub>6</sub> octahedral units yields different crystallographic forms. Fig. 1 shows the XRD patterns of as-prepared  $\alpha$ -MnO<sub>2</sub> and  $\delta$ -MnO<sub>2</sub>. The characteristic peaks of  $\alpha$ -MnO<sub>2</sub> are at 12.5°, 17.9°, 28.7°, 37.4°, 41.8°, 49.6°, 56.4°, 60.3°, 65.1°, and 69.7°, corresponding to facet indexes of (110), (200), (310), (211), (301), (411), (600), (521), (002), and (541), respectively (JCPDS 44-0141). The diffraction pattern of  $\delta$ -MnO<sub>2</sub> differs greatly

from that of  $\alpha$ -MnO<sub>2</sub>. It has characteristic peaks at 12.3°, 24.9°, and 36.6°, with corresponding facet indexes of (001), (002), and (006), respectively (JCPDS 18-0802). MnO<sub>2</sub> crystallographic structures are strongly controlled by varying the molar ratio of KMnO<sub>4</sub>/MnSO<sub>4</sub>. When the  $\delta$ -MnO<sub>2</sub> is formed in the hydrothermal process with a high K<sup>+</sup> concentration, the high molar ratio of KMnO<sub>4</sub>/MnSO<sub>4</sub> results in the production of K<sub>x</sub>MnO<sub>2</sub>·yH<sub>2</sub>O, yielding the layered  $\delta$ -MnO<sub>2</sub> that contains K<sup>+</sup> [35,36].

Fig. 2a and b presents HRSEM images of  $\alpha$ -MnO<sub>2</sub> and  $\delta$ -MnO<sub>2</sub>, respectively. The morphology of  $\alpha$ -MnO<sub>2</sub> is that of a needle-like nanowire with a diameter of 20–30 nm and a length of 2–4 μm. The morphology of  $\delta$ -MnO<sub>2</sub> is that of petal-shaped nanosheets with a thickness of 5–10 nm. Many  $\delta$ -MnO<sub>2</sub> nanosheets are aggregated into shapes like hydrangea flowers, and the diameter of each cluster is 0.4–0.7 μm. Fig. 2c presents a TEM image of  $\alpha$ -MnO<sub>2</sub> with a diameter of 25 nm. The inset in Fig. 2c presents its selected area diffraction (SAD) pattern, which includes a couple of spots within rings that correspond to crystal planes, revealing that the  $\alpha$ -MnO<sub>2</sub> has a polycrystalline structure. Fig. 2d presents the enlarged TEM image with the clear lattice fringes of  $\alpha$ -MnO<sub>2</sub>. From these fringes, the *d*-spacing is 0.48–0.49 nm, as shown in the inset digital micrograph, corresponding to the *d*-spacing of the (200) plane, revealing that the growth direction of the nanowire during the hydrothermal process is along [011] direction. Fig. 2e displays a TEM image of  $\delta$ -MnO<sub>2</sub>, and the inset presents the corresponding SAD pattern. The SAD pattern includes a couple of very weak spot patterns within rings, revealing that the  $\delta$ -MnO<sub>2</sub> tends to be an amorphous structure. Wei et al. found that adding K<sup>+</sup> not only delayed the conversion of manganese ions to manganese dioxide, but also increased the phase transformation temperature [37]. They found that the MnO<sub>2</sub> nanostructures changed from highly crystalline to amorphous as the K<sup>+</sup> concentration increased. Fig. 2f presents the enlarged TEM image that shows clear lattice fringes of the  $\delta$ -MnO<sub>2</sub>. The calculated *d*-spacing is 0.67–0.70 nm, as shown in the inset digital micrograph. The ideal *d*-spacing of (002) of  $\delta$ -MnO<sub>2</sub> is 0.72 nm. The difference between these two values may be caused by the spherical aberration or the image distortion that originates in TEM.

Fig. 3a plots the CV curves of activated carbon (background), the  $\alpha$ -MnO<sub>2</sub> electrode, and the  $\delta$ -MnO<sub>2</sub> electrode, obtained at a scan rate of 5 mV s<sup>-1</sup> in the potential range of −0.2 to 0.8 V. Since all MnO<sub>2</sub> samples are mixed with activated carbon, the CV curve reveals that the capacitive property of activated carbon can be ignored compared to other samples. The specific capacitance of  $\alpha$ -MnO<sub>2</sub> electrode is 107.6 F g<sup>-1</sup>. In this work, the specific capacitance of  $\alpha$ -MnO<sub>2</sub> electrode is much lower than that, 297 F g<sup>-1</sup>, in the work of Devaraj and Munichandraiah [15]. Wei et al. found specific capacitances from 58 to 124 F g<sup>-1</sup> for their amorphous  $\alpha$ -MnO<sub>2</sub> samples [37]. The specific capacitance of  $\delta$ -MnO<sub>2</sub> electrode herein is 265.8 F g<sup>-1</sup>, which is almost 2.5 times that of  $\alpha$ -MnO<sub>2</sub> electrode. Fig. 3b presents the specific capacitances of  $\alpha$ -MnO<sub>2</sub> and  $\delta$ -MnO<sub>2</sub> electrodes at various scan rates. The  $\delta$ -MnO<sub>2</sub> electrode not only exhibits high specific capacitances but also maintains these high values much more effectively than the  $\alpha$ -MnO<sub>2</sub> electrode at high scan rates. Therefore, the  $\delta$ -MnO<sub>2</sub> electrode is selected herein for subsequent study as the positive electrode of the ASC.

Carbon-based materials are used in electrochemical double-layer capacitors which must have a high specific surface area, a high mesoporous volume, and a particular electrical conductivity. The carbonization temperature of CNF was set to 800 °C herein. Fig. 4a and b presents HRSEM images of the CNF electrode and the CNT-CNF electrode, respectively. Following the carbonization, the CNFs remain smooth and straight with diameters of 200–250 nm, as presented in the inset of Fig. 4a. However, the CNT-embedded CNFs are curled and have slightly rough surfaces, and their

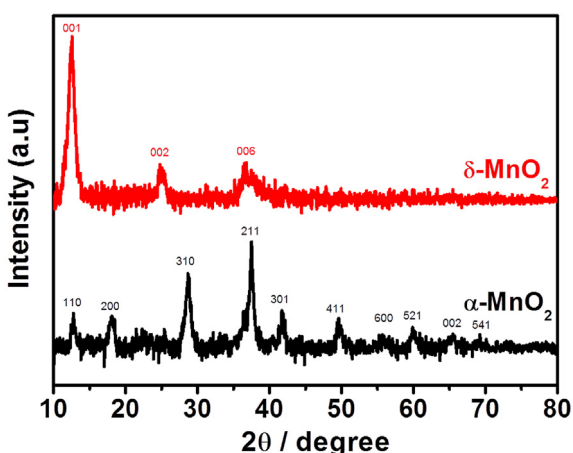
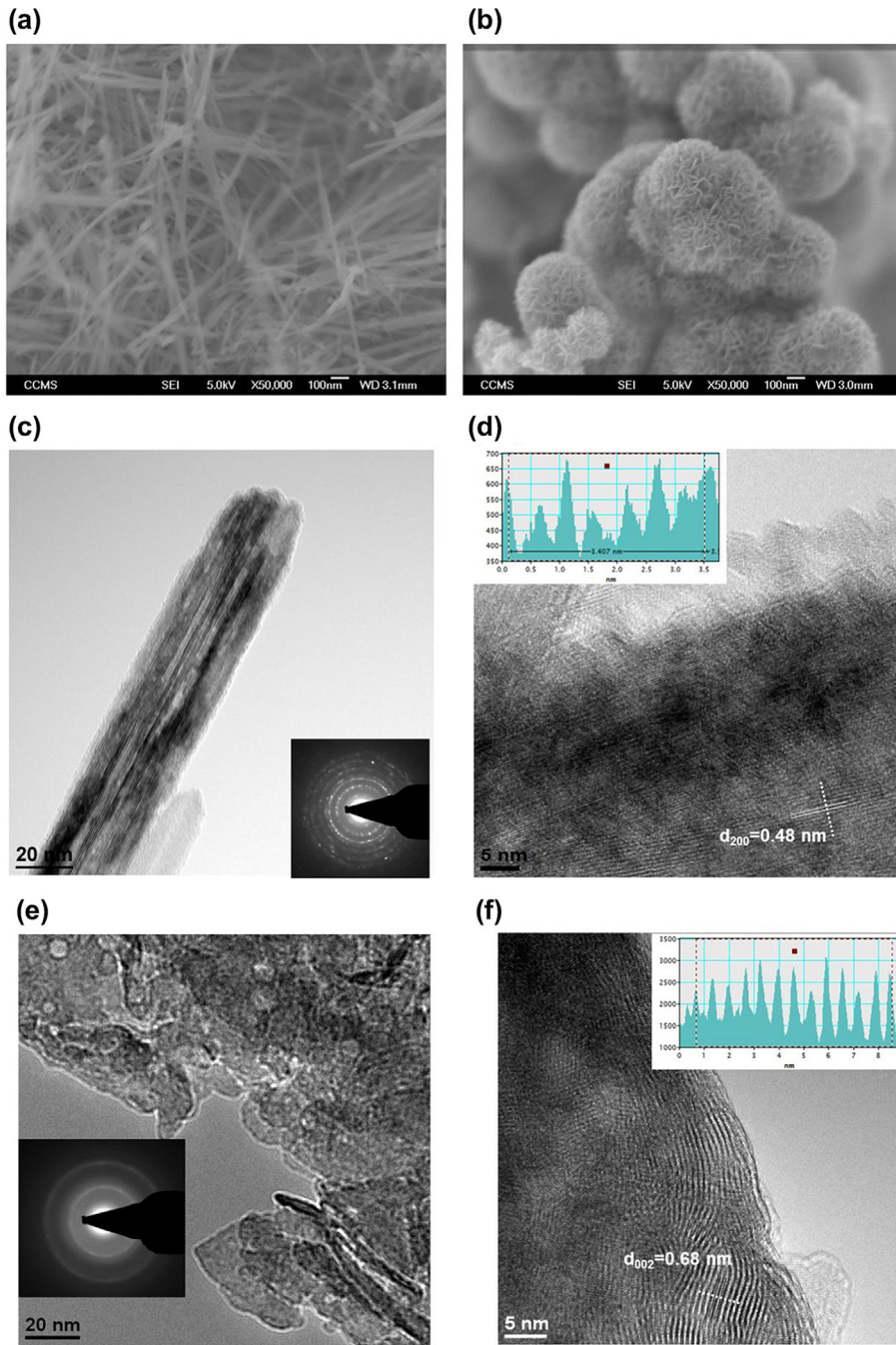


Fig. 1. XRD patterns of  $\alpha$ -MnO<sub>2</sub> and  $\delta$ -MnO<sub>2</sub>.



**Fig. 2.** HRSEM images of (a)  $\alpha$ -MnO<sub>2</sub> and (b)  $\delta$ -MnO<sub>2</sub>; TEM images of (c)  $\alpha$ -MnO<sub>2</sub> with the inset of SAD pattern and (d) the corresponding enlarged image with the inset of digital micrograph; TEM images of (e)  $\delta$ -MnO<sub>2</sub> with the inset of SAD pattern and (f) the corresponding enlarged image with the inset of digital micrograph.

diameters are increased to 300–350 nm, as presented in the inset of Fig. 4b. The additional CNTs in the CNFs may be responsible for this change, and these characteristics have been identified in elsewhere studies [38–40]. Since the CNTs have rigid tubular structures, when the slightly curved CNTs are added to them, the CNFs may form with the curvature of these added CNTs. Added the highly curved, winding or helical CNTs cannot be embedded in the CNFs, which therefore have the rough surfaces [32].

The electrical conductivity of the samples was determined in a two-electrode holder by performing an AC impedance analysis. The measurements of impedance reveal that the electrical conductivities of the CNF electrode and the CNT-CNF electrode are 9.5 and

52.6 S cm<sup>-1</sup>. Clearly, adding the CNTs to the CNT-CNF electrode greatly increases its electrical conductivity over that of the CNF electrode. A high electrical conductivity of the electrode is expected to result in low energy-loss during the charge/discharge cycles.

The surface properties of carbon-based materials strongly influence the electrochemical performance of double-layer capacitances. Table 1 summarizes the BET measurements of the CNF electrode and the CNT-CNF electrode. Therefore, the specific surface area and the specific pore volume of the CNT-CNF electrode exceed those of the CNF electrode.

Fig. 5a plots the capacitive characteristics of the CNT-CNF electrode and the CNF electrode at a scan rate of 5 mV s<sup>-1</sup>. The specific

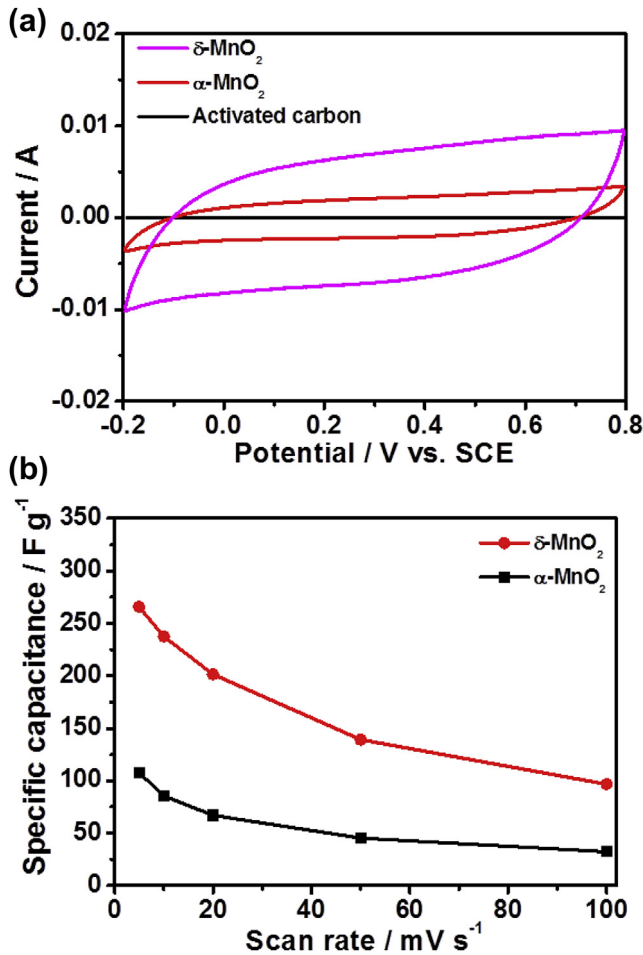


**Fig. 3.** (a) CV curves of activated carbon (background),  $\alpha\text{-MnO}_2$  electrode, and  $\delta\text{-MnO}_2$  electrode at a scan rate of 5 mV s<sup>-1</sup> in 0.5 M Na<sub>2</sub>SO<sub>4</sub>; (b) the specific capacitances of  $\alpha\text{-MnO}_2$  electrode and  $\delta\text{-MnO}_2$  electrode at various scan rates.

capacitances of these electrodes are 126.8 F g<sup>-1</sup> and 34.5 F g<sup>-1</sup>, respectively. The shapes of measured CV curves are a little distorted. Gao et al. obtained the similar shapes of measured CV curves of carbon nanotubes and carbon nanofibers composite film, and found that the radii of the hydrated cations may dominate the behavior of the electrical double-layer on carbon-based materials [41]. The CV curve of CNT-CNF electrode exhibits almost no deformation and no obvious oxidation/reduction peak, indicating that

**Table 1**  
Summary of BET and BJH properties of various samples.

Sample	$S_{\text{BET}}$ (m <sup>2</sup> g <sup>-1</sup> )	$V_{\text{Pore}}$ (cm <sup>3</sup> g <sup>-1</sup> )
CNF electrode	11.9	0.02
CNT-CNF electrode	50.2	0.156

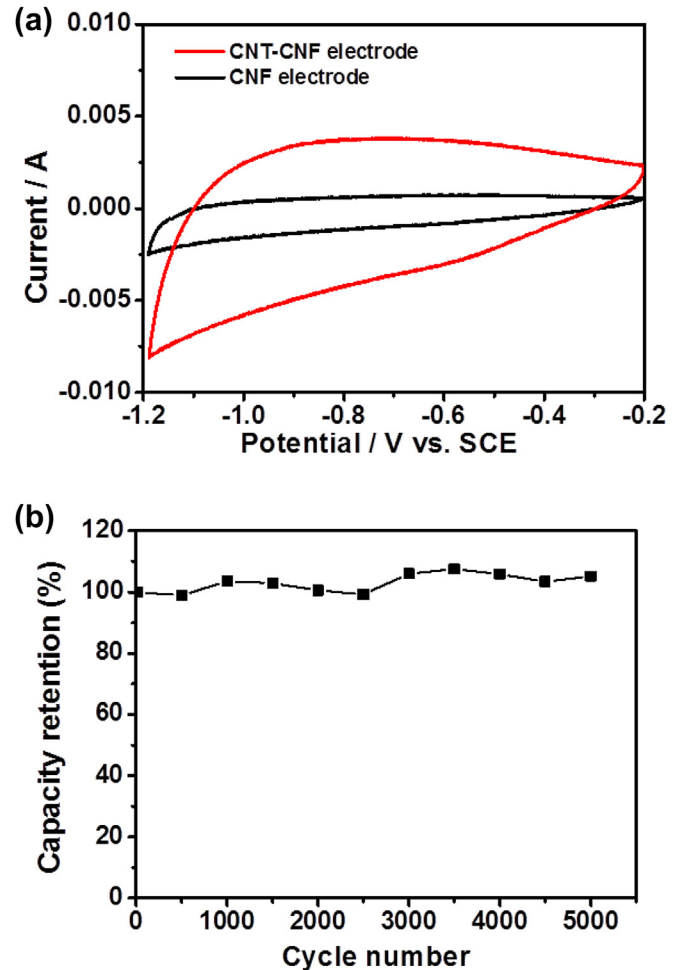


**Fig. 5.** (a) CV curves of CNT-CNF electrode and CNF electrode at a scan rate of 5 mV s<sup>-1</sup> in 0.5 M Na<sub>2</sub>SO<sub>4</sub>; (b) the cyclic test of CNT-CNF electrode between the potential range of -1.2 to -0.2 V.

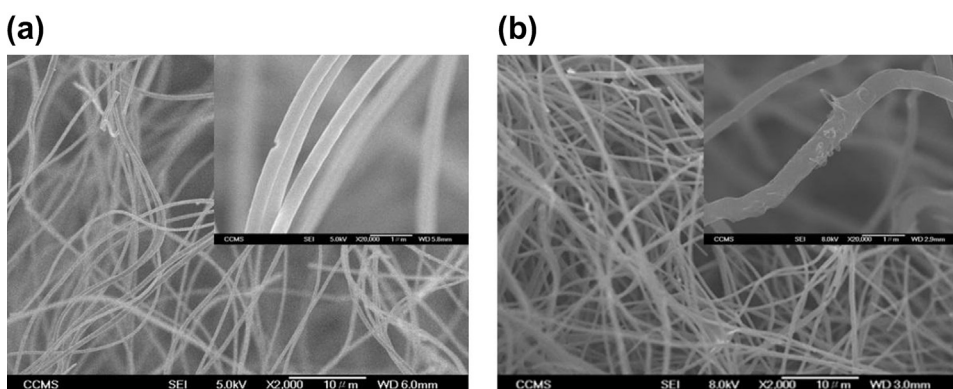


**Fig. 4.** HRSEM images of (a) CNF electrode and (b) CNT-CNF electrode.

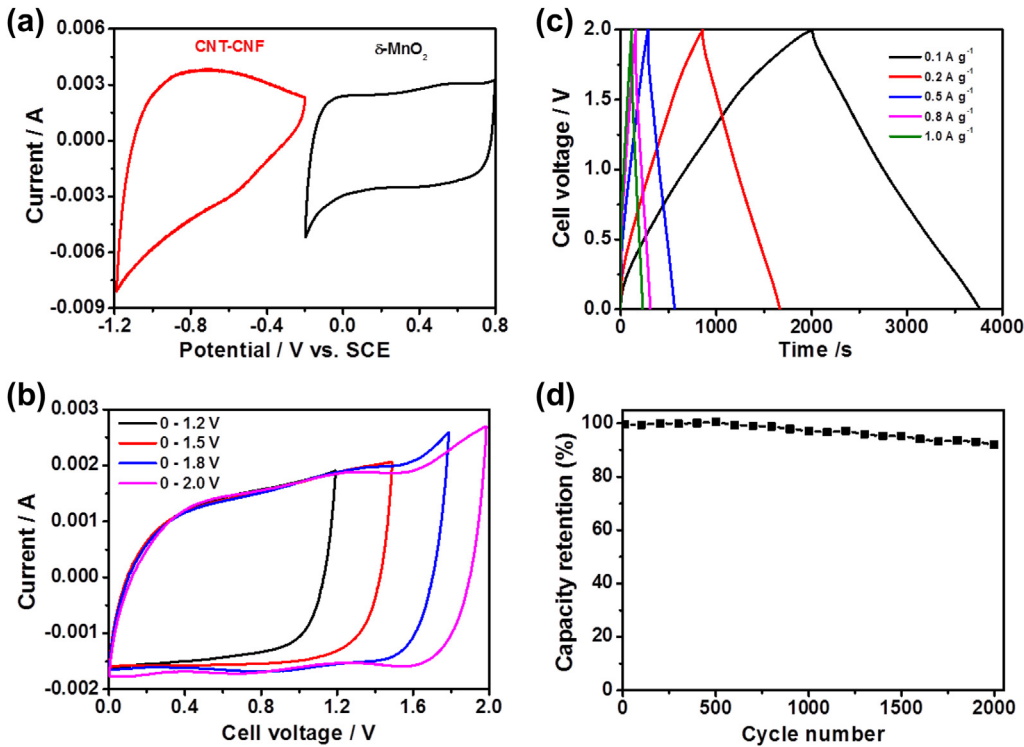


**Fig. 6.** (a) Comparison of CV curves of  $\delta\text{-MnO}_2$  electrode and CNT-CNF electrode in a three-electrode cell at a scan rate  $5 \text{ mV s}^{-1}$ ; (b) CV curves of  $\delta\text{-MnO}_2/\text{CNT-CNF}$  ASC at different voltage window at a scan rate of  $5 \text{ mV s}^{-1}$ ; (c) charge/discharge curves of  $\delta\text{-MnO}_2/\text{CNT-CNF}$  ASC at various current densities; (d) the cyclic test of  $\delta\text{-MnO}_2/\text{CNT-CNF}$  ASC between the potential range of  $0\text{--}2.0 \text{ V}$ .

ions ( $\text{Na}^+$ ) are adsorbed by the surface of the electrode, forming an electrical double-layer, owing to a Coulombic interaction rather than an electrochemical reaction [42].

One of the most important characteristics of an electrochemical double-layer capacitor is its durable cyclic performance. A cyclic test of the CNT-CNF electrode is carried out at a scan rate of  $50 \text{ mV s}^{-1}$  in the potential range  $-1.2$  to  $-0.2 \text{ V}$ . Fig. 5b plots the capacity retention as a function cycle number. After 5000 cycles, the capacity retention is 100%. Restated, the embedding of CNTs in the CNFs may stabilize the carbon structures in the electrochemical charge/discharge process.

Fig. 6a compares CV curves of the  $\delta\text{-MnO}_2$  electrode and the CNT-CNF electrode in  $0.5 \text{ M Na}_2\text{SO}_4$  in a three-electrode cell at a scan rate  $5 \text{ mV s}^{-1}$ . The stable potential range of the CNT-CNF electrode is  $-1.2$  to  $-0.2 \text{ V}$  and that of the  $\delta\text{-MnO}_2$  electrode is  $-0.2$  to  $0.8 \text{ V}$ . Accordingly, the sum of the potential ranges of the two electrodes is  $2.0 \text{ V}$ , indicating that they can potentially be used in a high-voltage ASC that operates at  $2.0 \text{ V}$  with  $0.5 \text{ M Na}_2\text{SO}_4$ . Since the two electrodes have different specific capacitance, the mass ratio between the two electrodes is given by the equation:

$$\frac{m_+}{m_-} = \frac{C_- \times \Delta E_-}{C_+ \times \Delta E_+} \quad (3)$$

where  $m$  is the mass of the active material in the electrode;  $C$  is the specific capacitance, and  $\Delta E$  is the range of potentials over which the charge/discharge process occurs. The charge/discharge process of the  $\delta\text{-MnO}_2/\text{CNT-CNF}$  ASC was examined using a two-electrode cell. Fig. 6b plots the CV curves of the  $\delta\text{-MnO}_2/\text{CNT-CNF}$  ASC for different voltage windows in the  $0.5 \text{ M Na}_2\text{SO}_4$  at a scan rate of  $5 \text{ mV s}^{-1}$ . The capacitive characteristics are favorable at cell voltages from  $1.0 \text{ V}$  to  $2.0 \text{ V}$ .

Galvanostatic charge/discharge measurements were made at various current densities to elucidate the electrochemical behaviors and determine the specific capacitances of the  $\delta\text{-MnO}_2/\text{CNT-CNF}$  ASC with  $0.5 \text{ M Na}_2\text{SO}_4$  at a cell voltage of  $2.0 \text{ V}$ , as presented in Fig. 6c. The charge curves are clearly symmetrical with the corresponding discharge curves, revealing that the  $iR$  drop in the charge/discharge process is very small [43]. Each curve reflects a highly linear relation between charge/discharge potential vs. time, indicating that the  $\delta\text{-MnO}_2/\text{CNT-CNF}$  ASC has excellent capacitive characteristics.

The specific capacitances and the energy densities are calculated from various discharge curves based on the total mass of the active materials on the two electrodes, whose power densities ( $P$ ) are given by Equations (1) and (4), and presented in Table 2. The energy density of the  $\delta\text{-MnO}_2/\text{CNT-CNF}$  ASC is  $52.22 \text{ Wh kg}^{-1}$  at a power density of  $100 \text{ W kg}^{-1}$ , and reaches  $30.74 \text{ Wh kg}^{-1}$  at  $1000 \text{ W kg}^{-1}$ .

$$P = \frac{E}{t} \quad (4)$$

where  $t$  is the discharge duration. Table 3 compares the results in this work are compared with those in the literature. The specific capacitance is mainly determined by the material property, which is also affected by the electrolyte, the applied current density, and

**Table 2**

The specific capacitive properties of the  $\delta\text{-MnO}_2/\text{CNT-CNF}$  ASC at various charge/discharge current density.

$I (\text{A g}^{-1})$	0.10	0.20	0.50	0.80	1.00
$C (\text{F g}^{-1})$	93.99	83.36	70.31	62.01	55.33
$E (\text{Wh kg}^{-1})$	52.22	46.31	39.06	34.45	30.74
$P (\text{W kg}^{-1})$	100.00	200.00	500.00	800.00	1000.00

**Table 3**Comparison of  $\text{MnO}_2//\text{carbon}$  ASCs from literature.

Positive electrode	Negative electrode	Electrolyte	Cell voltage (V)	$C (\text{F g}^{-1})$	$I (\text{A g}^{-1})$	$E (\text{Wh kg}^{-1})$	$P (\text{W kg}^{-1})$	Ref.
$\text{MnO}_2$	AC <sup>a</sup>	1.0 M $\text{Na}_2\text{SO}_4$	2.0	30.8	0.10	17.1	100	[51]
$\text{MnO}_2$	Graphene	1.0 M $\text{Na}_2\text{SO}_4$	2.0	45.5	0.10	25.2	100	[52]
$\text{MnO}_2$	Graphene	0.5 M $\text{Na}_2\text{SO}_4$	2.0	41.8	1.00	23.2	1000	[46]
$\text{MnO}_2/\text{GHCs}$	GHCS <sup>b</sup>	1.0 M $\text{Na}_2\text{SO}_4$	2.0	39.8	0.10	22.1	100	[53]
$\text{MnO}_2$	CNT	1.0 M $\text{Na}_2\text{SO}_4$	2.0	85.3	0.20	47.4	200	[44]
$\text{MnO}_2$	AC	1.0 M $\text{Na}_2\text{SO}_4$	2.0	50.6	0.10	28.1	100	[45]
$\text{MnO}_2/\text{CNT}$	CNT	1.0 M $\text{Na}_2\text{SO}_4$	2.0	27.6	0.10	15.3	100	[54]
$\text{NaMnO}_2$	AC	0.5 M $\text{Na}_2\text{SO}_4$	1.9	38.9	0.14	19.5	130	[55]
$\text{MnO}_2$	CNT-CNF	0.5 M $\text{Na}_2\text{SO}_4$	2.0	93.99	0.10	52.2	100	This work

<sup>a</sup> AC: activated carbon.<sup>b</sup> GHCS: graphitic hollow carbon sphere.

the assembling. Clearly, the energy density of  $\delta\text{-MnO}_2//\text{CNT-CNF}$  ASC is higher than or similar to those of most  $\text{MnO}_2//\text{carbon}$  ASCs in the literature. Jiang et al. demonstrated an  $\text{MnO}_2//\text{CNT}$  ASC with a 1.0 M  $\text{Na}_2\text{SO}_4$  of  $85.3 \text{ F g}^{-1}$  at  $0.20 \text{ A g}^{-1}$ , which value was a little higher than herein [44]. However, the specific capacitances of their ASC were only around  $50 \text{ F g}^{-1}$  and  $40 \text{ F g}^{-1}$  at  $0.80 \text{ A g}^{-1}$  and  $1.00 \text{ A g}^{-1}$ , respectively, which are lower than those herein, which are  $62.01 \text{ F g}^{-1}$  and  $55.33 \text{ F g}^{-1}$  at  $0.80 \text{ A g}^{-1}$  and  $1.00 \text{ A g}^{-1}$ , respectively.

Long-term cycling stability at a high scan rate is an essential property of a supercapacitor. Fig. 6d plots the capacity retention of the  $\delta\text{-MnO}_2//\text{CNT-CNF}$  ASC that is charged and discharged between 0 and 2.0 V at a scan rate of  $50 \text{ mV s}^{-1}$  as a function of the number of cycles. The  $\delta\text{-MnO}_2//\text{CNT-CNF}$  ASC exhibits superior electrochemical stability with 92% retention of the initial specific capacitance after 2000 cycles. This cycling performance is similar to those ASCs, such as  $\text{MnO}_2//\text{CNT}$  (90% retention after 1000 cycles) [44],  $\text{MnO}_2//\text{activated carbon}$  (84% retention after 1000 cycles) [45],  $\text{MnO}_2//\text{activated carbon}$  (88% retention after 1000 cycles) [13],  $\text{MnO}_2//\text{graphene}$  (87% retention after 2000 cycles; 83.4% retention after 5000 cycles) [46],  $\text{MnO}_2/\text{graphene}/\text{graphene}$  (79% retention after 1000 cycles) [47], CNTs/ $\text{MnO}_2//\text{CNTs/SnO}_2$  (92% retention after 1000 cycles) [48],  $\text{MnO}_2//\text{activated carbon}$  (93% retention after 100 cycles) [49], and  $\text{Ni(OH)}_2//\text{activated carbon}$  (82% retention after 1000 cycles) [50] ASCs. These results reveal that the  $\delta\text{-MnO}_2//\text{CNT-CNF}$  ASC herein has excellent electrochemical stability.

The high energy of the  $\delta\text{-MnO}_2//\text{CNT-CNF}$  ASC is attributable to the following. First, the  $\delta\text{-MnO}_2$  is composed petal-shaped nanosheets with a very small thickness of 5–10 nm; this thin structure ensures the high electrochemical utilization of active materials, providing a large surface area for attracting electroactive species. The size of  $\text{Na}^+$  is 0.4 nm in aqueous solution [56]. The interlayer distance in the  $\delta\text{-MnO}_2$  is approximately 0.67 nm, which may stabilize a significant amount of water and  $\text{Na}^+$  between  $\text{MnO}_6$  octahedral structures. The thin  $\delta\text{-MnO}_2$  ensures the high electrochemical utilization of active materials, providing a large surface for attracting electroactive species. Additionally, according to earlier studies [57–59], the crystalline  $\delta\text{-MnO}_2$  herein has an amorphous structure, favoring high capacitance. Second, an electrical double-layer capacitor should have large pores, a high surface area, and high electrical conductivity. The conventional negative electrode was composed of activated carbon that is mixed with binders, which were screen-printed on the nickel foil. Acetylene carbon black, whose BET surface area and electrical conductivity are  $65 \text{ m}^2 \text{ g}^{-1}$  and  $0.0025 \text{ S cm}^{-1}$ , respectively, is typically used in negative electrodes [25]. Recent works have used activated carbon with a large surface area ( $1000\text{--}3500 \text{ m}^2 \text{ g}^{-1}$ ) and carbon nanomaterials with high electrical conductivity (such as CNT, graphene,  $10^4\text{--}10^6 \text{ S cm}^{-1}$ ) [1,23,26,27,60]. Compared to those materials, the CNT-CNF electrode herein does not have a significant surface area

or high electrical conductivity. However, it has a good network structure, and the CNFs therein form conductive chains and the embedded CNTs improve the electrical conductivity of the CNFs, resulting in low energy loss during the charge/discharge. Third, the energy density of the supercapacitor is proportional to the square of the operating cell voltage. The  $\delta\text{-MnO}_2//\text{CNT-CNF}$  ASC can operate up to 2 V with very good long-term cycling stability in an aqueous neutral electrolyte.

#### 4. Conclusion

This work demonstrates an ASC using petal-like  $\text{MnO}_2$  nanosheets and CNT-embedded polyacrylonitrile-based carbon nanofibers as the positive and negative electrodes, respectively. It has a voltage window of 2.0 V and exhibits a specific capacitance of  $93.99 \text{ F g}^{-1}$  with a corresponding energy density of  $52.22 \text{ Wh kg}^{-1}$  at a current density of  $0.1 \text{ A g}^{-1}$ . The capacitive properties of  $\alpha\text{-MnO}_2$  and  $\delta\text{-MnO}_2$  are firstly evaluated. As-prepared  $\delta\text{-MnO}_2$  is formed of very thin nanosheets with amorphous structure, and has a higher capacitance than as-prepared  $\alpha\text{-MnO}_2$ . Second, the CNT-CNF electrode has a favorable double-layer capacitance owing to its network structure. Apart from the synergistic effects of the two superior electrodes, the  $\delta\text{-MnO}_2//\text{CNT-CNF}$  ASC exhibits not only excellent electrochemical performance but also excellent cycling stability, retaining 92% of the initial specific capacitance after 2000 cycles, making it an ASC with potential for use in various applications.

#### Acknowledgment

The authors would like to thank the Taiwan Textile Research Institute for financially supporting this research. Technical support by Dr. Chuan-Ming Tseng from NanoCore, the Core facilities for nanoscience and nanotechnology at Academia Sinica in Taiwan, is acknowledged. Ted Knoy is appreciated for his editorial assistance.

#### References

- [1] P. Simon, Y. Gogotsi, Nat. Mater. 7 (2008) 845–854.
- [2] S.W. Lee, B.M. Gallant, H.R. Byon, P.T. Hammond, Y. Shao-Horn, Energy Environ. Sci. 4 (2011) 1972–1985.
- [3] E. Frackowiak, Phys. Chem. Chem. Phys. 9 (2007) 1774–1785.
- [4] D. Cericola, R. Kotz, A. Wokaun, J. Power Sources 196 (2011) 3114–3118.
- [5] Y. Wang, Z. Hong, M. Wei, Y. Xia, Adv. Funct. Mater. 22 (2012) 5185–5193.
- [6] P.W. Ruch, D. Cericola, A. Foelske, R. Kotz, A. Wokaun, Electrochim. Acta 55 (2010) 2352–2357.
- [7] L. Demarconnay, E. Raymundo-Pinero, F. Beguin, Electrochim. Commun. 12 (2010) 1275–1278.
- [8] M.P. Bichat, E. Raymundo-Pinero, F. Beguin, Carbon 48 (2010) 4351–4361.
- [9] Y. Wang, J. Cao, Y. Zhou, J.-H. Ouyang, D. Jia, L. Guo, J. Electrochim. Soc. 159 (2012) A579–A583.
- [10] Z. Fan, J. Yan, T. Wei, L. Zhi, G. Ning, T. Li, F. Wei, Adv. Funct. Mater. 21 (2011) 2366–2375.
- [11] K. Naoi, P. Simon, Interface 17 (2008) 34–37.

- [12] C. Xu, F. Kang, B. Li, H. Du, J. Mater. Res. 25 (2010) 1421–1432.
- [13] V. Khomenko, E. Raymundo-Pinero, F. Beguin, J. Power Sources 153 (2006) 183–190.
- [14] T. Brousse, M. Toupin, R. Dugas, L. Athouel, O. Crosnier, D. Belanger, J. Electrochem. Soc. 153 (2006) A2171–A2180.
- [15] S. Devaraj, N. Munichandraiah, J. Phys. Chem. C 112 (2008) 4406–4417.
- [16] Y. Show, K. Imaizumi, Diamond Relat. Mater. 16 (2007) 1154–1158.
- [17] J.D. Wiggins-Camacho, K.J. Stevenson, J. Phys. Chem. C 113 (2009) 19082–19090.
- [18] X. Zhao, B.T.T. Chu, B. Ballesteros, W. Wang, C. Johnston, J.M. Sykes, P.S. Grant, Nanotechnology 20 (2009) 065605.
- [19] D. Chunsheng, P. Ning, Nanotechnology 17 (2006) 5314.
- [20] J. Wang, Y. Xu, X. Chen, X. Sun, Compos. Sci. Technol. 67 (2007) 2981–2985.
- [21] C.G. Liu, H.T. Fang, F. Li, M. Liu, H.M. Cheng, J. Power Sources 160 (2006) 758–761.
- [22] K.H. An, W.S. Kim, Y.S. Park, J.-M. Moon, D.J. Bae, S.C. Lim, Y.S. Lee, Y.H. Lee, Adv. Funct. Mater. 11 (2001) 387–392.
- [23] P. Simon, A. Burke, Interface 17 (2008) 38–43.
- [24] A.S. Arico, P. Bruce, B. Scrosati, J.-M. Tarascon, W. van Schalkwijk, Nat. Mater. 4 (2005) 366–377.
- [25] K. Kinoshita, Carbon: Electrochemical and Physicochemical Properties, Wiley, New York, 1988.
- [26] L.L. Zhang, R. Zhou, X.S. Zhao, J. Mater. Chem. 20 (2010) 5983–5992.
- [27] L.L. Zhang, X.S. Zhao, Chem. Soc. Rev. 38 (2009) 2520–2531.
- [28] H. Wang, Y. Wang, Z. Hu, X. Wang, ACS Appl. Mater. Interfaces 4 (2012) 6827–6834.
- [29] J.-W. Lang, X.-B. Yan, W.-W. Liu, R.-T. Wang, Q.-J. Xue, J. Power Sources 204 (2012) 220–229.
- [30] S.K. Nataraj, K.S. Yang, T.M. Aminabhavi, Prog. Polym. Sci. (Oxford) 37 (2012) 487–513.
- [31] Z. Dong, S.J. Kennedy, Y. Wu, J. Power Sources 196 (2011) 4886–4904.
- [32] Q. Guo, X. Zhou, X. Li, S. Chen, A. Seema, A. Greiner, H. Hou, J. Mater. Chem. 19 (2009) 2810–2816.
- [33] Z. Zhou, X.-F. Wu, H. Fong, Appl. Phys. Lett. 100 (2012) 023115-1–023115-4.
- [34] H.-C. Hsu, C.-H. Wang, S.K. Nataraj, H.-C. Huang, H.-Y. Du, S.-T. Chang, L.-C. Chen, K.-H. Chen, Diamond Relat. Mater. 25 (2012) 176–179.
- [35] Y. Yang, C. Huang, J. Solid State Electrochem. 14 (2010) 1293–1301.
- [36] X. Wang, Y. Li, Chem. Eur. J. 9 (2003) 300–306.
- [37] C. Wei, C. Xu, B. Li, H. Du, D. Nan, F. Kang, J. Power Sources 225 (2013) 226–230.
- [38] W. Salalha, Y. Dror, R.L. Khalfin, Y. Cohen, A.L. Yarin, E. Zussman, Langmuir 20 (2004) 9852–9855.
- [39] Y. Dror, W. Salalha, R.L. Khalfin, Y. Cohen, A.L. Yarin, E. Zussman, Langmuir 19 (2003) 7012–7020.
- [40] H. Hou, J.J. Ge, J. Zeng, Q. Li, D.H. Reneker, A. Greiner, S.Z.D. Cheng, Chem. Mater. 17 (2005) 967–973.
- [41] Y. Gao, L. Pan, H. Li, Y. Zhang, Z. Zhang, Y. Chen, Z. Sun, Thin Solid Films 517 (2009) 1616–1619.
- [42] M.-W. Ryoo, J.-H. Kim, G. Seo, J. Colloid Interface Sci. 264 (2003) 414–419.
- [43] C.-L. Liu, K.-H. Chang, C.-C. Hu, W.-C. Wen, J. Power Sources 217 (2012) 184–192.
- [44] H. Jiang, C. Li, T. Sun, J. Ma, Nanoscale 4 (2012) 807–812.
- [45] X. Zhang, X. Sun, H. Zhang, D. Zhang, Y. Ma, Mater. Chem. Phys. 137 (2012) 290–296.
- [46] H. Gao, F. Xiao, C.B. Ching, H. Duan, ACS Appl. Mater. Interfaces 4 (2012) 2801–2810.
- [47] Z.-S. Wu, W. Ren, D.-W. Wang, F. Li, B. Liu, H.-M. Cheng, ACS Nano 4 (2010) 5835–5842.
- [48] C. Yu, C. Masarapu, J. Rong, B.M. Wei, H. Jiang, Adv. Mater. 21 (2009) 4793–4797.
- [49] M.S. Hong, S.H. Lee, S.W. Kim, Electrochim. Solid-State Lett. 5 (2002) A227–A230.
- [50] J.-W. Lang, L.-B. Kong, M. Liu, Y.-C. Luo, L. Kang, J. Solid State Electrochem. 14 (2010) 1533–1539.
- [51] X. Zhang, P. Yu, H. Zhang, D. Zhang, X. Sun, Y. Ma, Electrochim. Acta 89 (2013) 523–529.
- [52] J. Cao, Y. Wang, Y. Zhou, J.-H. Ouyang, D. Jia, L. Guo, J. Electroanal. Chem. 689 (2012) 201–206.
- [53] Z. Lei, J. Zhang, X.S. Zhao, J. Mater. Chem. 22 (2012) 153–160.
- [54] H. Zhang, Y. Huang, B. Xu, G. Cao, ECS Solid State Lett. 1 (2012) M1–M3.
- [55] Q.T. Qu, Y. Shi, S. Tian, Y.H. Chen, Y.P. Wu, R. Holze, J. Power Sources 194 (2009) 1222–1225.
- [56] R.N. Reddy, R.G. Reddy, J. Power Sources 124 (2003) 330–337.
- [57] G. Wang, L. Liu, L. Zhang, J. Zhang, Ionics 19 (2013) 689–695.
- [58] Y. Munaiah, B.G. Sundara Raj, T. Prem Kumar, P. Ragupathy, J. Mater. Chem. A 1 (2013) 4300–4306.
- [59] D. Yang, J. Power Sources 228 (2013) 89–96.
- [60] H. Pan, J. Li, Y.P. Feng, Nanoscale Res. Lett. 5 (2010) 654–668.